JOURNAL OF Applied Polymer SCIENCE

Polyimide/Substituted Polyaniline-Copolymer-Nanoclay Composite Thin Films with High Damping Abilities

J. Longun, J. O. Iroh
Materials Engineering Program, School of Aerospace Systems, College of Engineering and Applied Science, University of Cincinnati, 2600 Clifton Avenue, Cincinnati, Ohio 45221
Correspondence to: J. O. Iroh (E-mail: irohj@ucmail.uc.edu)

ABSTRACT: Polyimide (PI)/poly(*N*-ethyl aniline-*co*-aniline-2-sulfonic acid)–clay (SPNEAC) nanocomposite films containing water-soluble SPNEAC were successfully synthesized. Atomic force microscopy studies showed a homogeneous distribution of coated clay particles in the PI matrix. The particle sizes varied between about 50 nm and about 220 nm in height and 6–7 μm in length in the nanocomposite containing 5 wt % SPNEAC. Average surface roughnesses of 0.253 and 34.9 nm were obtained for neat PI and the 5 wt % SPNEAC–PI nanocomposite, respectively. Dynamic mechanical spectrometry was used to study the viscoelastic transitions and their temperatures. The dynamic mechanical spectrometry results show a decreasing glass-transition temperature of the nanocomposites with increasing SPNEAC weight fraction. The area under the α-transition peak, which is associated with damping and impact energy, increased with increasing SPNEAC weight fraction. The impact energy of the nanocomposites was estimated with a viscoelastic model. It increased with increasing SPNEAC weight fraction, and a maximum value of 84.9 mJ was obtained. The viscoelastic model was based on the area under the α-transition peak, rubbery plateau modulus, and sample volume. A 5 wt % addition of SPNEAC improved the impact energy of neat PI films by 300%. Scanning electron micrographs of the nanocomposite films showed a less compact cross-sectional morphology. © 2012 Wiley Periodicals, Inc. J. Appl. Polym. Sci. 000: 000–000, 2012

KEYWORDS: clay; coatings; composites; polyimides; nanocomposites

Received 14 March 2011; accepted 9 January 2012; published online
DOI: 10.1002/app.36794

INTRODUCTION

Polymer-based nanocomposites continue to gain great attention because of the desirable properties of polyimide (PI), such as its high thermooxidative stability, its excellent mechanical properties and solvent resistance, and the excellent barrier properties of clay. Lan et al.[1] successfully dispersed organoclay in a PI matrix to form PI/clay nanocomposites. They reported improved gas barrier properties and a decreased coefficient of thermal expansion in the presence of organoclay. Since then, a lot of work has been dedicated to the study of PI/clay nanocomposites.[2–7] The most recent studies have focused on the use of PI-based nanocomposites for humidity sensing,[8] electrical conductivity,[9–11] gas separation,[12–14] corrosion protection,[15,16] and high-temperature coatings.[17,18]

PI has often been blended with polyaniline to improve its electrical conductivity and corrosion resistance. For example, Liangchai et al.[19] prepared a PI/polyaniline blend and studied its corrosion protection properties. They reported the improved corrosion protection of mild carbon steel in the presence of a PI–polyaniline polyblend. Sua et al.[20] also performed pervaporation and gas permeability studies on PI/polyaniline blends, and they reported a decreased gas permeability in PI/polyaniline blends compared to neat PI.

However, one important aspect, often less explored, of the blending of PI with other polymers is the effect of blending on the thermomechanical properties of PI and, more importantly, the damping ability. Damping in polymers results from energy dissipation during deformation.[21] Traditionally, the damping enhancement of composites/nanocomposites is improved by viscoelastic polymer materials,[22] carbon-fiber prepregs[23] and magnetostrictive particles.[24] Despite the ability of viscoelastic polymers to enhance the damping ability of composite/nanocomposite materials, they compromise the stiffness and strength.[25] Magnetostrictive materials, such as ferromagnetic materials, undergo a change in shape due to magnetization and have been used as active transducers and passive dampers.[26] Carbon nanotubes (CNTs), too, have recently been used to enhance the damping of nanocomposite materials.[27] Also, because of the high aspect ratio, high stiffness, and large surface area of CNTs, it is expected that one can achieve energy

Applied Polymer SCIENCE

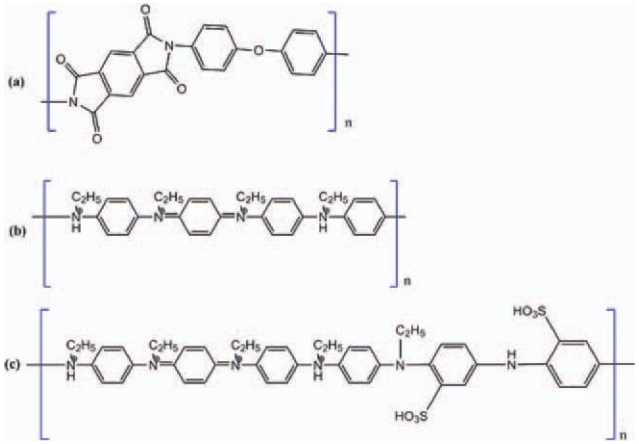

Figure 1. Schematic of the structures of the (a) PI, (b) partially oxidized PNEA, and (c) SPNEA copolymer. [Color figure can be viewed in the online issue, which is available at wileyonlinelibrary.com.]

dissipation and structural damping by taking advantage of the interfacial friction between CNTs and the polymer matrix and between CNT particles.[28] However, the cost associated with CNTs and magnetostrictive particles presents a major impediment in their use as damping agents.

In this study, we successfully synthesized PI/poly(*N*-ethyl aniline-*co*-aniline-2-sulfonic acid)–clay (SPNEAC) nanocomposite films with significantly high damping abilities. The damping agent that was used in this study was SPNEAC. On the basis of the results, not only did the copolymer (Figure 1) significantly improve the damping ability of the nanocomposite films, but it did so without sacrificing the thermal stability and mechanical strength of the PI matrix.

EXPERIMENTAL

Materials

The reagents used in this study were as follows. Aniline-2-sulfonic acid (A2-S; 95% purity), *N*-ethyl aniline (NEA; 98% purity), and *N*-methyl pyrrolidone (NMP; 99% purity) were purchased from Sigma-Aldrich Co. (St. Louis, MO). Oxalic acid (99% purity), dodecyl benzene sulfonic acid monohydrate (98% purity), 4,4-oxydianiline (ODA; 99% purity), pyromellitic dianhydride (PMDA; 99% purity), and ammonium persulfate (99% purity) were also purchased from Sigma-Aldrich. Cloisite 30B clay was purchased from Southern Clay, Inc. All of the reagents listed previously were analytical grade. Doubly distilled and deionized water was also used in this process.

Synthesis of the SPNEAC Copolymer

Synthesis of the SPNEAC composite was carried out via a single polymerization process. Amounts of 5.41 g of A2-S, 3.94 g of NEA, 1.125 g of oxalic acid, 4.36 g of dodecyl benzene sulfonic acid monohydrate, and 0.585 g of Cloisite 30B clay were added to a beaker containing 150 mL of doubly distilled water; this was followed by ultrasonication for 3–5 min. Stirring was continued for 30 min with a mechanical stirrer, after which Cloisite 30B clay was added to the resulting mixture. Then, the mixture was stirred for 30 min, and 4.36 g of ammonium persulfate was added dropwise to the mixture followed by stirring for 24 h. The product was filtered, dried in a vacuum oven at 120°C, and then stored in a desiccator.

Synthesis of the Poly(amic acid)/Poly(*N*-ethyl aniline-*co*-aniline-2-sulfonic acid)–Clay (SPNEAC–PAA) Solution

An amount of 5.1608 g of ODA was added to 100 mL of NMP in a round-bottom flask, and the mixture was stirred for 30 min by means of a mechanical stirrer. SPNEAC prepared in the previously discussed second step was added to the ODA solution, and this was followed by vigorous stirring. After 6 h of stirring, 5.6216 g of PMDA was added to the mixture, and stirring was continued for 15 h. Solutions were prepared with 0.25, 0.5, 1, 2, and 5% SPNEAC weight fractions.

Preparation of the SPNEAC–PI Nanocomposite Films

PI/SPNEAC films were prepared by the casting of an SPNEAC–PAA solution onto a glass substrate followed by drying in a vacuum oven at 120°C for 2 h and at 200°C for 1 h.

Characterization Method

Dynamic mechanical spectroscopy was used to study the viscoelastic behavior of the nanocomposite films. Measurements were performed on 20 × 10 × 0.06 mm^3 films from 25 to 550°C with an EXSTAR6000 (Seiko Instruments, Inc.) under tensile loading at a heating rate of 5°C/min and a frequency of 1 Hz. Thermal transitions were studied with a DSC6200 (Seiko Instruments). Wide-angle X-ray diffraction (WAXD) was used to study the structure of the SPNEAC/PI nanocomposite membranes. X-ray diffraction was carried out with Cu K radiation sources at a wavelength of 1.54 Å in a diffraction angle range of $2\theta = 0.5$ to 15°C. The cross-sectional morphology of the films was studied with scanning electron microscopy (SEM; FEI XL30 field effect environmental scanning electron microscope (FEG ESEM)). During SEM sample preparation, thin films were immersed in liquid nitrogen and then fractured with a pair of tweezers to expose their cross-sectional area. A Polaron SC7640 sputter coater was used to coat the samples with silver. The microstructure of the nanocomposites was studied with atomic force microscopy (AFM). AFM measurements were conducted with a Nanoscope Dimension 3100 Controller (Digital Instruments) operating in the tapping mode. Si cantilevers manufactured by Nanoworld were used with a force constant of 2.8 Nm and a nominal resonance frequency of 75 KHz. The phase signal was set to zero at the resonance frequency of the tip. The tapping frequency was set to 10% lower than the resonance frequency. The drive amplitude was about 360 mV, and the amplitude set point was 1.4 V. Thermal studies were performed with a Netzsch STA 409 PC Luxx model thermogravimetric analyzer at 10°C/min, and ultraviolet–visible (UV–vis) spectroscopy (DSC 6000 Seiko Instruments) was used to study the optical properties of poly(aniline-2-sulfonic acid) (PA2S), PNEA, and poly(*N*-ethyl aniline-*co*-aniline-2-sulfonic acid) (SPNEA). Measurements were performed with a U-3000 series spectrometer with wavelength range of 190–900 nm (Bio-Rad, Hurcules, CA).

RESULTS AND DISCUSSION

UV–Vis Spectroscopy

Figure 2 shows the UV–vis spectra of PA2S, poly(*N*-ethyl aniline) (PNEA), the PA2S–PNEA blend, and SPNEA in NMP. All

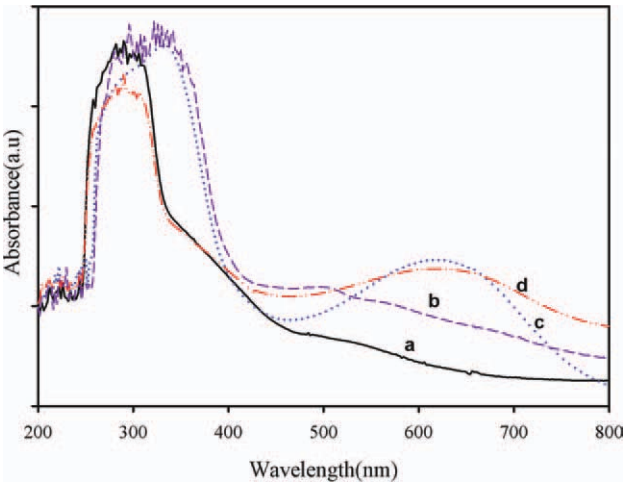

Figure 2. UV–vis spectra of the (a) PA2S, (b) SPNEA, (c) PA2S–PNEA blend, and (d) PNEA showing optical absorbance with respect with wavelength. [Color figure can be viewed in the online issue, which is available at wileyonlinelibrary.com.]

of the samples showed UV–vis absorption at about 280 nm to about 330 nm; this was attributed to π–π^* transitions in the benzenoid structure. The area under the peak in the 280–330-nm region increased in the following order: PA2S < PNEA < SPNEA; this was believed to be due to an increase in the conjugation length of the polymers. PA2S showed a shoulder between 320 and 480 nm and a weak and broad peak at about 560 nm, believed to be due to polaron n–π^* transitions and n–π^* transitions in the quinoid structure. We believe the UV–vis absorbance between 320 and 480 nm was blueshifted because of the presence of SO_3H groups in PA2S. PNEA showed UV–vis absorption at 280–420 and 450–800 nm. The absorbance peak at about 600 nm was characteristic of the emeraldine base form of polyaniline. The UV–vis absorption of the homopolymer blends showed a shoulder between 320 and 480 nm and an absorption peak between 450 and 800 nm, similar to PA2S and PNEA, respectively. The UV–vis spectrum of the copolymer showed absorptions centered at about 320 m and 560 nm due to π–π^* transitions in the benzenoid structure and n–π^* transitions in the quinoid structure, respectively. The UV–vis absorption of the copolymer greatly differed from that of the blend; this confirmed that the polymer in question was indeed a copolymer and not a mixture of PNEA and PA2S.

Functional Group Analysis (Fourier Transform Infrared Spectroscopy)

Figure 3(a,b) shows the attenuated total reflectance spectra of the neat PI and the PI containing SPNEAC at 70 and 250°C, respectively. Typical PI peaks were observed at 1780 cm^{-1}, due to asymmetric C=O stretching; 1360 cm^{-1}, due to C—N stretching of the tertiary amine; and 722 cm^{-1}, due to symmetric C=O stretching. Another notable observation worth mentioning was that typical imide absorption peaks (at 722, 1360, and 1780 cm^{-1}) were still prominent in both the neat PI [Figure 3(a)] and the PI containing 5 wt % SPNEAC [Figure 3(b)] at 70 and 250°C; this indicated that the presence of SPNEAC in the PI matrix did not affect the structure of the imide ring. Typical SPNEA absorption bands due to the quinoid group (1600 cm^{-1}) and benzenoid structure (1500 cm^{-1}) were not easily observed because of overlap with other PI absorbance bands in this region.

DSC Studies

Figure 4(a,b) shows the second-run DSC thermograms and their derivatives for PA2S, PNEA, and SPNEA. The glass-transition temperature (T_g) and melting temperature (T_m) were obtained. On the basis of the derivative of the DSC thermograms; the T_g's of PA2S, PNEA, and SPNEA were determined to be 71.6, 141.1, and 126.7°C, respectively. PNEA showed a T_m at 227.5°C, and SPNEA showed two T_m's at 227.1 and 246.6°C, whereas poly (aniline 2-sulfonic acid) (P2AS) showed no T_m. The theoretical T_g of the copolymer, calculated with the Fox equation for random copolymers, was obtained as 132.7 ± 5°C. The similarity between the theoretical T_g and the experimentally determined T_g of the copolymer indicated that the synthesized polymer was a copolymer and not a mixture of PNEA and PA2S, as shown

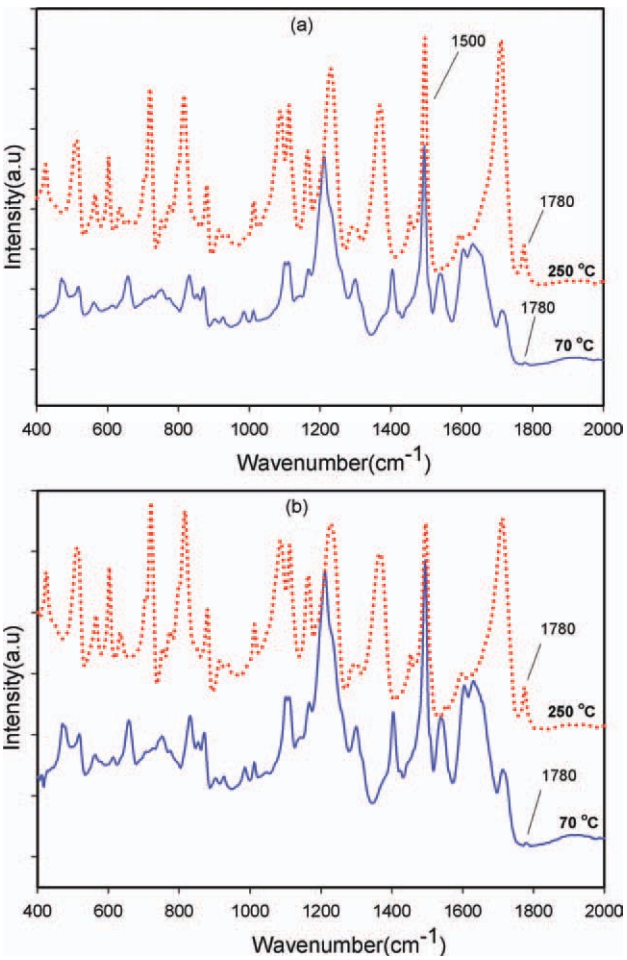

Figure 3. Plot of the attenuated total reflectance–Fourier transform infrared spectra of (a) neat PI at 70°C and (b) 5 wt % SPNEAC–PI at 70 and 250°C, respectively. [Color figure can be viewed in the online issue, which is available at wileyonlinelibrary.com.]

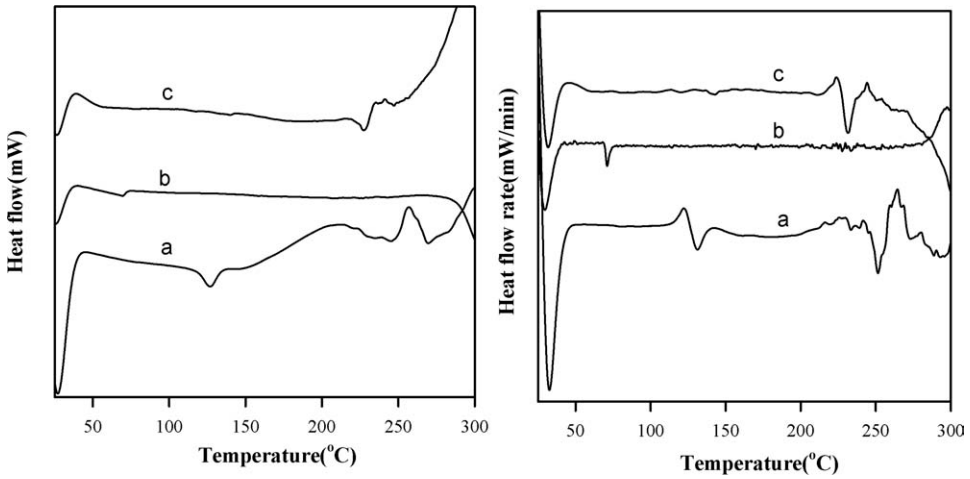

Figure 4. DSC thermogram and derivative DSC thermograms for (a) SPNEA, (b) PA2S, and (c) PNEA showing thermal transitions. The T_g's of SPNEA, PA2S, and PNEA were 126.7, 71.6, and 141.1°C.

by the UV–vis results. This observation was in agreement with the UV–vis results:

$$\frac{1}{T_g} = \frac{W_A}{T_g A} + \frac{W_B}{T_g B}$$

where W_A is weight fraction of polymer *A*; W_B is weight fraction of polymer *B*. *A* and *B* represent polymer *A* and polymer *B* in the copolymer.

Thermogravimetric Studies

Thermogravimetric analysis (TGA) was performed on the SPNEAC/PI composite films, where the weight loss due to the discharge of degradation products was monitored as a function of temperature, as shown in Figure 5(a,b). Studies were performed on PI and PIs containing 0.5, 2, and 5 wt % SPNEAC, and as shown in Table I, the thermal degradation temperature (T_d) increased with increasing weight fraction of SPNEAC up to a maximum value of 600.3°C at 2 wt % and then decreased to a value of 584.5°C at 5 wt % SPNEAC. The clay was thermally stable, and its modification with the substituted polyaniline copolymer enhanced the clay–PI compatibility, which then limited heat transport within the nanocomposite material. The decrease in T_d at 5 wt % was a result of increased porosity, as observed in the SEM images (shown later). The weight retention percentages of PI and the SPNEAC/PI nanocomposite taken at 250, 450, and 650°C were plotted as a function of SPNEAC weight percentage, as shown in Figure 5(b). At 250°C, the weight retention for PI and the SPNEAC/PI nanocomposite was about 97%; at 450°C, the weight retention decreased to about 92% and then increased slightly with increasing weight percentage of SPNEAC. The weight retentions values obtained at 650°C were 63.29, 66.34, 68.55, and 64.48% for PI and PIs containing 0.5, 2, and 5 wt % SPNEAC, respectively. The weight retention at 650°C became more sensitive to the SPNEAC weight percentage,

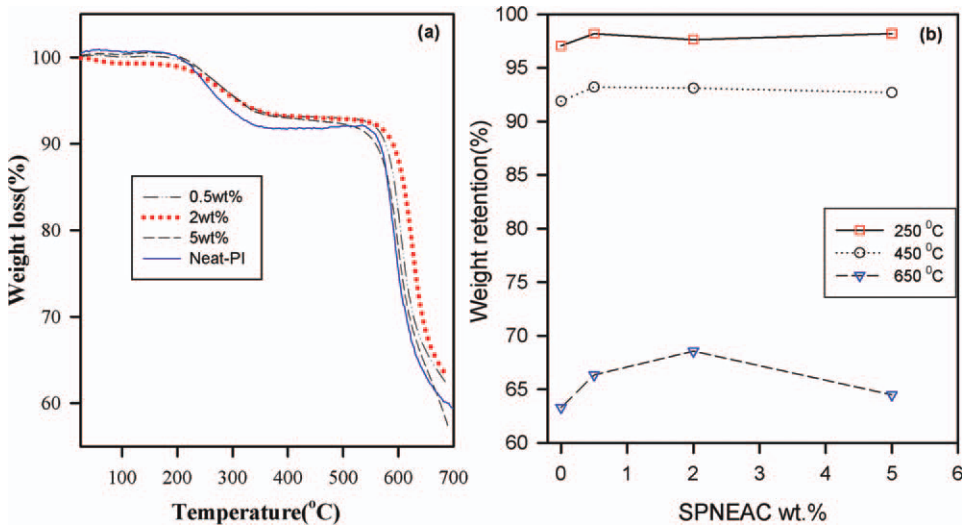

Figure 5. TGA results showing the (a) percentage weight loss versus temperature and (b) plot of the weight retention of the neat PI and PI nancomposite containing 0.5, 2, and 5 wt % SPNEAC nanocomposite films. A weight retention of about 60% was observed after 700°C. [Color figure can be viewed in the online issue, which is available at wileyonlinelibrary.com.]

Table I. Values of E', Rubbery Plateau Modulus (E_r), Tan δ, T_g (°C), and Tan δ Area of the Neat PI and SPNEAC–PI Nanocomposite Films

wt %	E' (GPa)	E_r (MPa)	Tan δ	T_g (°C)	Tan δ area	Impact energy (mJ)
0	1.2	0.39	116.05	405.9	4.450	20.8
0.25	1.9	0.35	112.49	406.3	5.500	23.1
0.5	2.3	0.48	129.55	399.6	5.800	33.1
1	1.7	0.37	136.56	398.9	7.800	34.1
2	1.1	0.42	137.28	394.3	8.125	41.0
5	0.93	0.67	135.29	376.9	10.55	84.9

and it tended to increase with increasing SPNEAC weight percentage up to 2 wt %, after which a significant decrease was observed at 5 wt %; this was attributed to increased porosity.

Dynamic Mechanical Analysis

The variation in the dynamical mechanical behavior of the PI and PI nanocomposites with SPNEAC were studied. The γ, β, and α transitions of neat PI are illustrated in Figure 6, and the corresponding T_γ, T_β, and T_α were about 50, 250, and 406°C, respectively. The storage modulus (E') and tan δ of neat PI and PI containing between 0.1 and 5 wt % SPNEAC are plotted against temperature in Figures 7(a,b) and 8(a,b).

E′

The room-temperature E' values [Figure 9(a)] of the samples increased with increasing amount of SPNEAC up to a maximum of 2.3 ± 0.025 GPa (∼ 47.8% increase) for 0.5 wt % SPNEAC and then decreased to a minimum value of 0.93 ± 0.020 GPa (∼ 22.5% decrease) for 5 wt % SPNEAC, compared to 1.2 GPa for the neat PI matrix. E' decreased sharply in the rubbery region, and this phenomenon was sensitive to the SPNEAC loading, with 5 wt % SPNEAC–PI showing the lowest α-transition temperature of 376.9°C. Even after we accounted for statistical error, the addition of SPNEAC at low amounts (≤0.5 wt %) produced a reinforcement effect on the PI matrix.

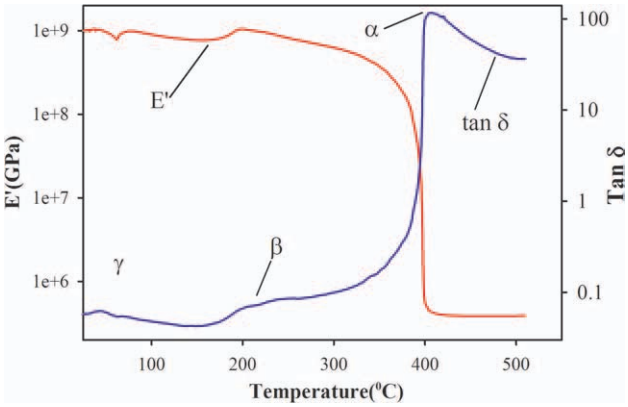

Figure 6. Graph of the neat PI showing E' and tan δ with respect to the temperature. The γ, β, and α transitions are indicated. γ and β were secondary transitions due to the vibration and stretching of side groups, respectively, whereas α was due to the mass movement of chains, and it signified the T_g of PI. [Color figure can be viewed in the online issue, which is available at wileyonlinelibrary.com.]

T_g

There was a considerable shift in the α-transition peak (Figure 8), the glass–rubber transition temperature. T_g [Figure 10(a) and Table II] decreased with increasing SPNEAC content. The decrease in T_g, however, was less pronounced at lower SPNEAC loadings when compared to PI containing higher SPNEAC weight fractions. The glass-region E' was highest for the SPNEAC–PI containing a low SPNEAC concentration. The dramatic decreases in T_g and E' at higher SPNEAC loading may have been related to the substituted polyaniline copolymer

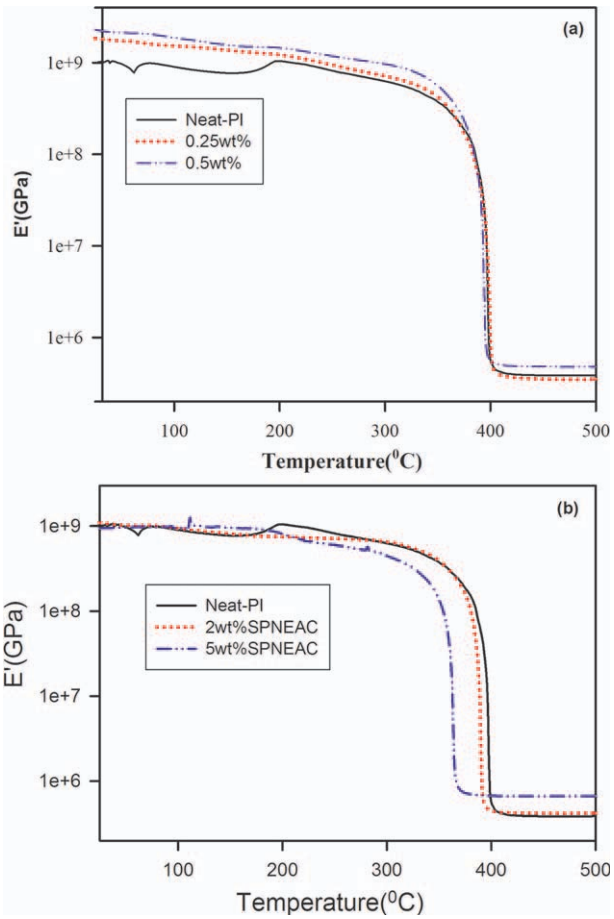

Figure 7. Plot of E' versus the temperature of (a) the neat PI (0.25 and 0.5 wt %) and (b) neat PI (2, and 5 wt %) SPNEAC-PI nanocomposite films showing the variation of E' with SPNEAC loading. [Color figure can be viewed in the online issue, which is available at wileyonlinelibrary.com.]

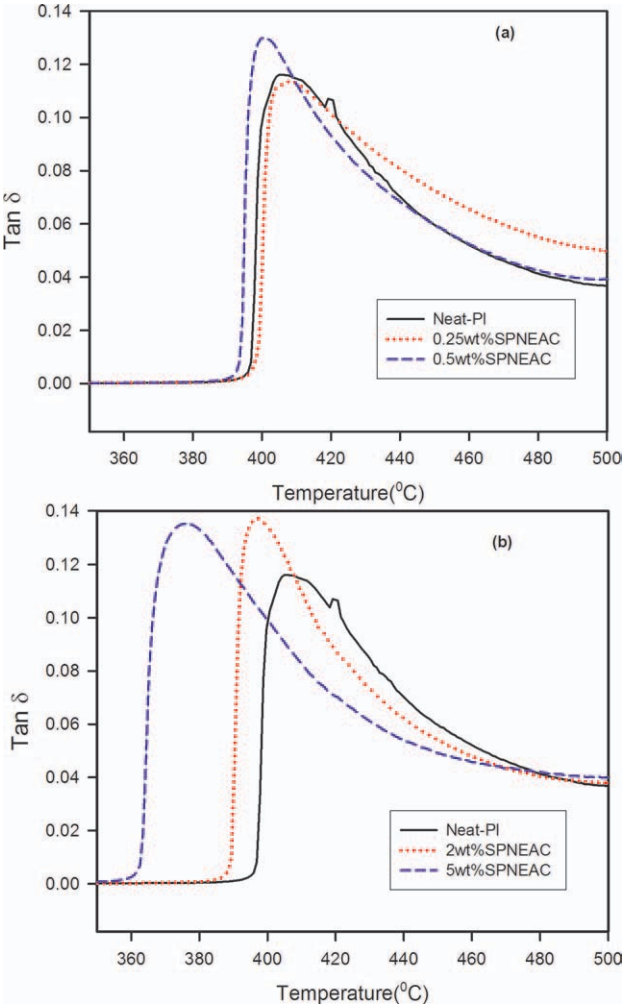

Figure 8. Plot of tan δ versus the temperature of (a) the neat PI (0.25 and 0.5 wt %) and (b) neat PI (2, and 5 wt %) SPNEAC-PI nanocomposite films showing the variation of tan δ with SPNEAC loading. [Color figure can be viewed in the online issue, which is available at wileyonlinelibrary.com.]

playing the role of a plasticizer. Another reason for the decreases in E' and T_g may have been the increased porosity, and this explanation was supported by the SEM images shown in Figure 11(b–d), which suggested an open and less compact morphology at high SPNEAC loadings ($\geq$0.5 wt %). For 5 wt % SPNEAC–PI, in particular, loosely bound nanosized nodules were spread throughout the cross-sectional area. These nodules were also observed on the surface of the samples on the AFM micrographs [Figure 12 (bottom)]. The presence of the nanonodules may play have played a role in increasing the flexibility and, thereby, decreasing the T_g of the SPNEAC/PI nanocomposite.

Damping

Viscoelastic materials are those materials that display both elastic and viscous behaviors. Elastic materials obey Hooke's law [eq. (1)], in which an instantaneous relationship between the stress and strain exists. When elastic materials are subjected to stress, they recover instantaneously when the stress is removed:

$$F = -kx \tag{1}$$

where F is the force applied, x is the displacement, and k is a spring constant.

On the other hand, viscous materials have a time-dependent relationship between the stress and strain such that when they are subjected to stress and the stress is removed, they do not recover fully. For an elastic material subjected to sinusoidal deformation, the stress and strain [eqs. (2a) and (2b)] are in phase, meaning that the phase angle (δ) is zero. For a viscous material, on the other hand, the strain is 90° out of phase with the stress; therefore, $\delta = 90°$. Viscoelastic materials display both elastic and viscous components and exhibit behavior between the two extremes. In this case, δ is between 0 and 90°:

$$\varepsilon = \varepsilon_0 \sin(\omega t) \tag{2a}$$

$$\sigma = \sigma_0 \sin(\omega t + \delta) \tag{2b}$$

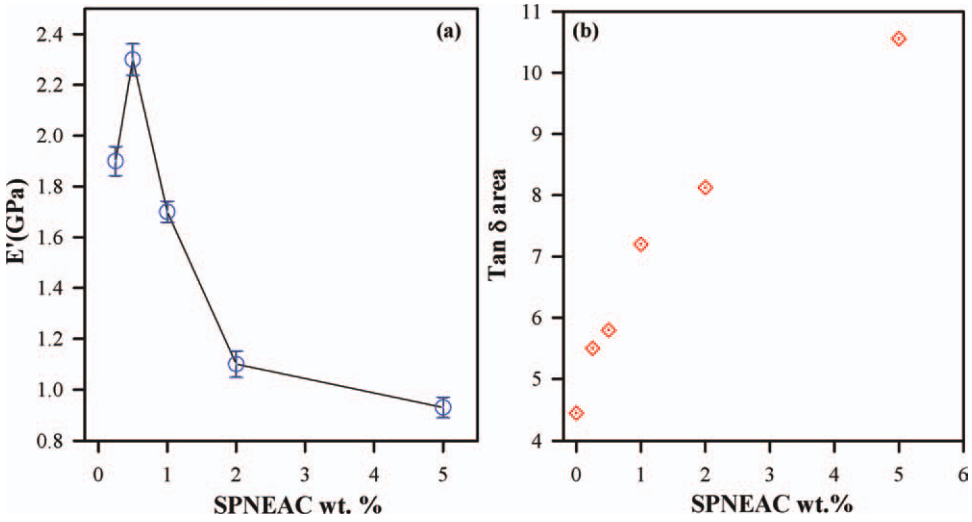

Figure 9. Graph showing (a) E' and (b) tan δ area versus the SPNEAC loading for neat-PI, and the 0.25, 0.5, 1, and 2 and 5 wt % SPNEAC-PI nanocomposite films. The area under tan δ increased with SPNEAC loading. [Color figure can be viewed in the online issue, which is available at wileyonlinelibrary.com.]

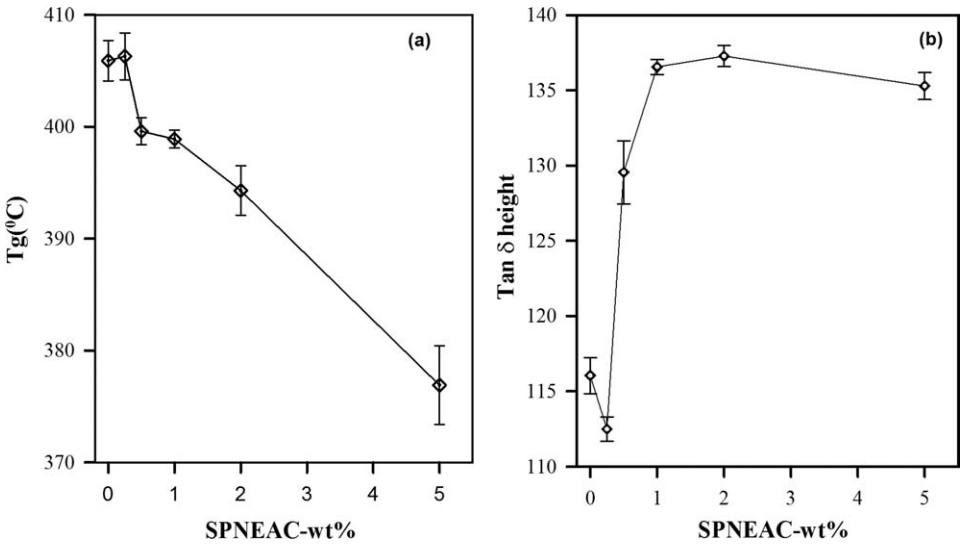

Figure 10. Plot showing T_g and tan δ height versus the SPNEAC weight percentage for neat PI and the 0.25, 0.5, 1, 2, and 5 wt % SPNEAC–PI nanocomposite films. T_g decreased with SPNEAC loading, whereas the tan δ height increased with the SPNEAC loading.

where ω is the frequency and t is time in seconds. The stress–strain relationship can be defined by E' and E'' as follows:

$$\sigma = \sigma_0 E' \sin(\omega t) + \varepsilon_0 E'' \cos(\omega t) \quad (2c)$$

$$E' = \frac{\sigma_0}{\varepsilon_0} \cos\delta \quad (2d)$$

$$E'' = \frac{\sigma_0}{\varepsilon_0} \sin\delta \quad (2e)$$

$$\tan\delta = \frac{E''}{E'} \quad (2f)$$

where E'' is the loss modulus, σ and σ_0 represent the sinusoidal stress and the initial stress. Tan δ, which is the ratio of E'' to E', represents the material's ability to absorb and dissipate energy and is associated with damping.

The effects of the temperature and composition on the height of tan δ was studied, and the results are shown [Figures 8 and 10(b)]. The height of tan δ is indicative of the material damping ability, and in the case of the SPNEAC/PI nanocomposite, the height of tan δ increased with increasing SPNEAC loading, except at a 0.25 wt % SPNEAC loading. The height of tan δ increased sharply from 116.5 for neat PI to a maximum value of 137.28 at a 2 wt % SPNEAC loading. This remarkable increase in damping ability at higher SPNEAC loading could be attributed to the open and loose structure [Figure 11(c)] of the SPNEAC/PI nanocomposite film; this is believed to have enhanced the relaxation ability of the nanocomposite, a phenomenon also observed in the decreasing T_g values. At 0.25 wt % SPNEAC loading, the structure [Figure 11(b)] of the SPNEAC/PI nanocomposite was dense and compact, and this was believed to hinder chain motion by reducing the overall relaxation space available to the PI chains.

Table II. T_d and Weight Retention (%) of the Neat PI and SPNEAC/PI Nanocomposites at 250, 450, and 650°C

wt %	250°C	450°C	650°C	T_d (°C)
0	97.06	91.87	63.30	561.5
0.5	98.18	93.20	66.34	595.4
2	97.62	94.10	68.55	600.3
5	98.19	92.69	64.49	594.5

Viscoelastic Model

For a viscoelastic material subjected to a single-frequency mechanical stress, dissipation from the mechanical energy into heat energy per cycle [$\Delta W(\omega)$] is given by[29]

$$\Delta W(\omega) = \int_0^{2\pi/\omega} [\sigma(\omega)\varepsilon(\omega)\partial t] \quad (3a)$$

$$= \omega\sigma_0\varepsilon_0 \int_0^{2\pi/\omega} [\cos\omega t \sin\omega t \cos\delta + \sin^2\omega t \sin\omega t \sin\delta]\partial t \quad (3b)$$

$$= \pi\varepsilon_0^2(\omega)\tan\delta E' \quad (3c)$$

$$\tan\delta = \frac{\Delta W(\omega)}{\pi\varepsilon_0^2(\omega)E'} \quad (3d)$$

$$\tan\delta = \frac{E''}{E'} \quad (3e)$$

where $\sigma(\omega)$ is the stress function, $\varepsilon(\omega)$ is the resultant strain function, ε_0 is the amplitude and δ is the phase angle between the stress and strain. E'' is the loss modulus and E' is the storage modulus.

Using the tan δ curve, we correlated the impact strength (σ_{imp}) of the neat PI and the SPNEAC–PI nanocomposite with the area under the tan δ curve [eq. (3a)], as proposed by Wada et al.:[30]

Applied Polymer SCIENCE

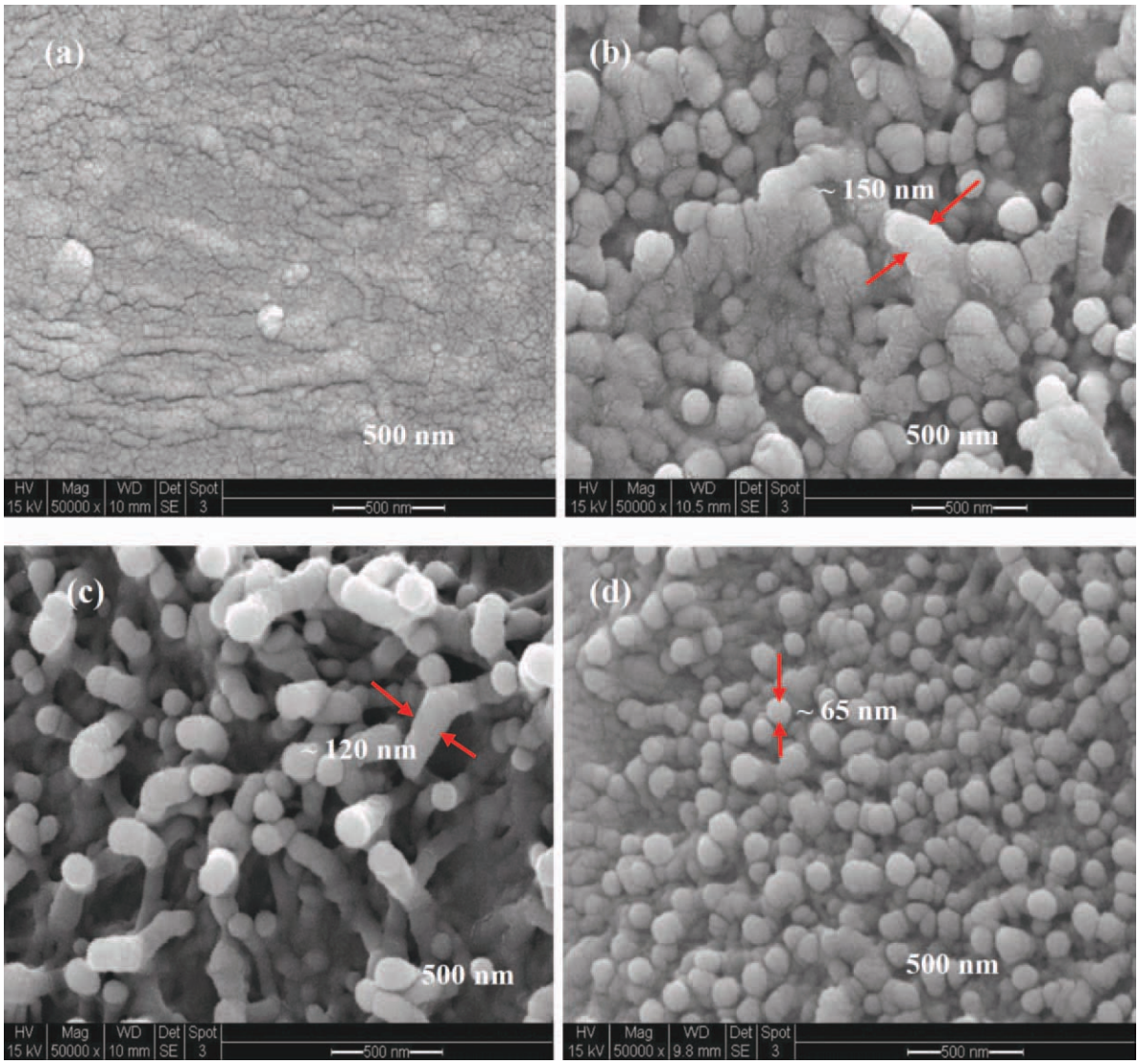

Figure 11. SEM micrographs of the (a) neat-PI and PI nanocomposite containing (b) 0.25, (c) 0.5, and (d) 5 wt % at 50,000× magnification showing cross-sectional morphology. With increasing SPNEAC loading, an open/less compact morphology with discrete features was observed. [Color figure can be viewed in the online issue, which is available at wileyonlinelibrary.com.]

$$\sigma_{\text{imp}} \propto \int_{T_0}^{T_t} (\tan\delta)\partial T \tag{4a}$$

However, in this case, we specifically focused on the area under the α-transition curve. With the relationship in eq. (3d), the impact energy could be expressed as follows:

$$\sigma_{\text{imp}} \propto \int_{T_0}^{T_t} \left[\frac{\Delta W(\omega)}{\pi \varepsilon_0^2(\omega) E'}\right] \partial T \tag{4b}$$

where T is temperature in Kelvin, T_0 is the reference temperature, taken to be the onset of the α-transition region because values of tan δ below this onset are very small, and T_t is the final temperature, taken to be 500°C. The values of the area under the α-transition curve are shown in Table II.

The area under the tan δ curve was calculated by the fitting of two polynomial equations into parts 1 and 2 of the tan δ curve, as typified in Figure 8(a). The total area under the curve was obtained by integration as follows:

$$\text{Total area} = \int_{x_1}^{x_2} [f(1)]\partial x + \int_{x_1}^{x_2} [f(2)]\partial x \tag{5}$$

where $f(1)$ and $f(2)$ stand for eqs. (1) and (2), respectively, and x_1 and x_2 are the lower and upper temperature limits, respectively.

The area under the tan δ curve has been reported to be a good indicator of the total energy absorbed by a material during deformation[31,32] and corresponds to the degree of molecular motion that enables the material to absorb and dissipate energy. The total energy absorbed (tan δ area), measured by the area under the α-transition peak, can be correlated with the impact strength.[26,32–34] Because the impact strength (proportional to the tan δ area) is related to viscoelastic relaxations, the region within the α-transition has the largest tan δ area and, therefore,

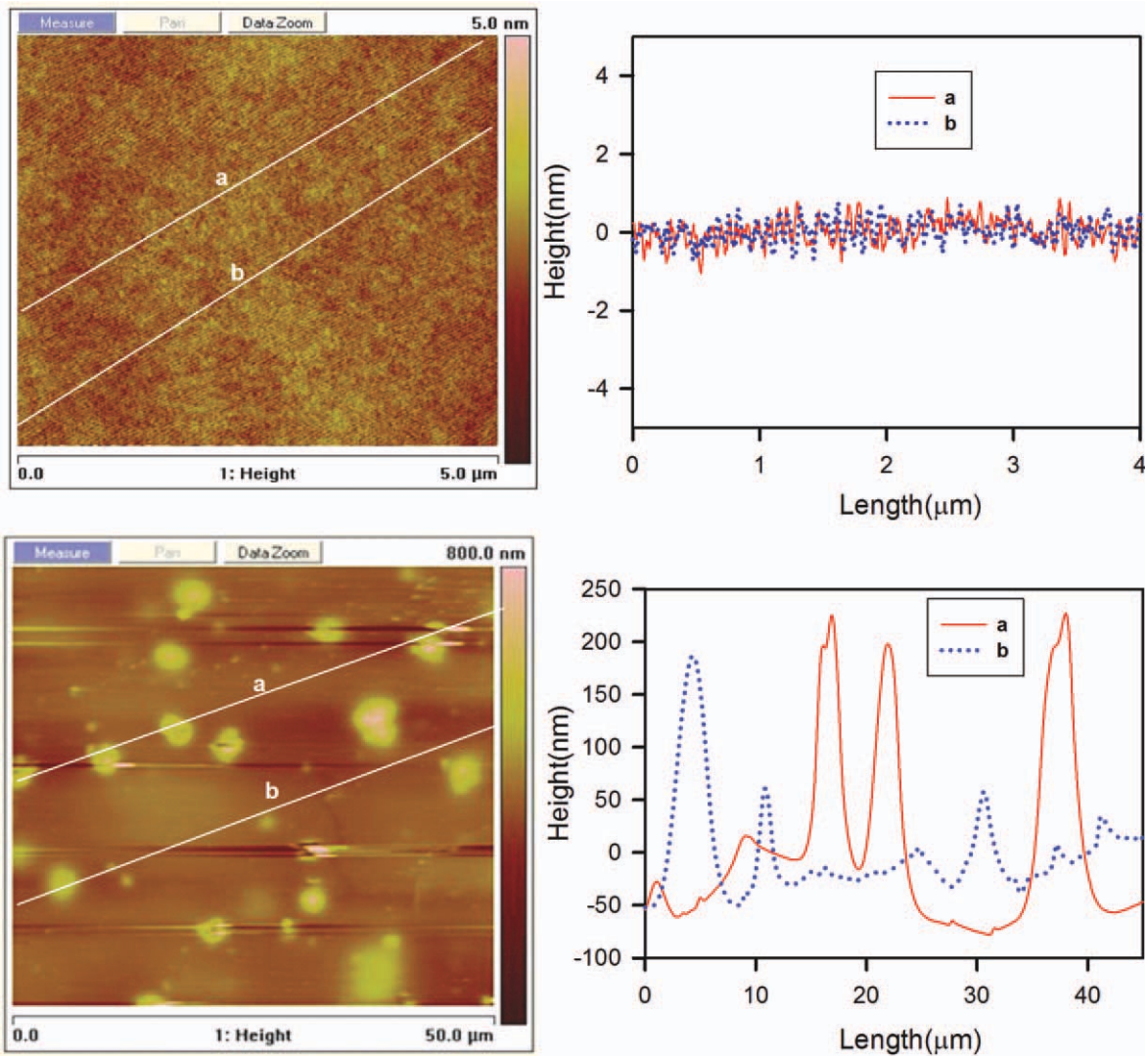

Figure 12. AFM images of the 5 wt % SPNEAC-PI nanocomposite (bottom) and neat-PI (top) showing height profile of the films performed in tapping mode. Discrete features between about 50 to about 220 nm in height and 6.7 μm in length were observed throughout the nanocomposite surface. [Color figure can be viewed in the online issue, which is available at wileyonlinelibrary.com.]

the largest impact strength because of increased viscoelastic relaxation.

As shown in Figure 9(b), the area under the α-transition curve increased with increasing SPNEAC loading. This phenomenon was attributed to the increased flexibility of SPNEAC and the porous and open morphology of the SPNEAC-filled PI matrix. This explanation was supported by the decreasing T_g and increasing α-transition peak area [Figure 9(b)] as the SPNEAC concentration was increased.

Estimation of the Impact Energy

The impact energy in joules (Table II) was estimated by the assignment of a proportionality constant (K) and the solution of eq. (5a) as follows:

$$\sigma_{\text{imp}} = K \int_{T_0}^{T_t} (\tan\delta)\partial T \tag{6}$$

where K is the product of the rubbery plateau modulus (MPa; Table II) and the volume of the film (m^3). The impact energy (Table II) increased with increasing SPNEAC loading, as predicted by the area under the α-transition peak.

WAXD Study

Figure 13 shows the WAXD diffraction spectra of the clay and SPNEAC/PI nanocomposites. The WAXD spectrum of clay powder showed a sharp diffraction peak at a low diffraction angle (2θ) of 4.76°, which corresponded to an interlayer spacing (d-spacing) of 18.47 Å. The d-spacing of Cloisite 30B nanoclay is significantly higher than the d-spacing for mineral clay (Na+ clay), which is 10.5 Å. The significant expansion of the interlayer spacing for Cloisite 30B clay was due to the insertion of the alkylated ammonium ion into the clay gallery. The WAXD spectrum of PI showed a broad diffraction peak at a diffraction angle of 18.87°, which corresponded to a d-spacing of 4.70 Å. It was noted that the PI derived from PMDA and ODA was an

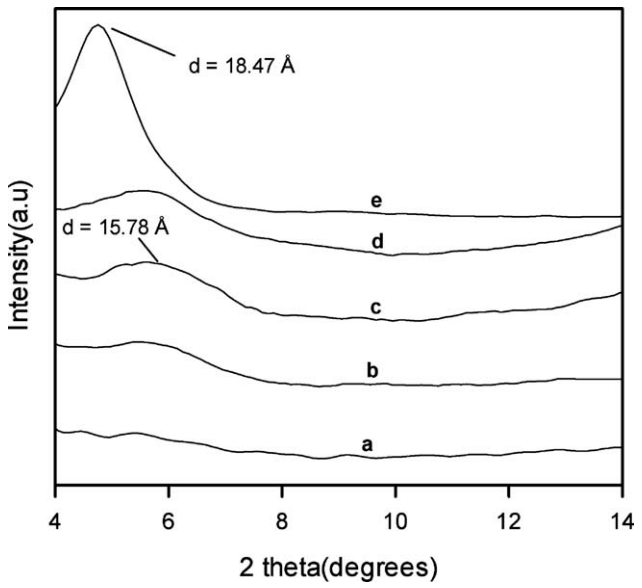

Figure 13. WAXD diffractogram for the (a) neat PI and PIs containing (b) 0.5, (c) 2 and (d) 5 wt % SPNEAC.

amorphous thermoplastic and, therefore, did not show any angle diffraction peaks between diffraction angles of 4 and 14°. The WAXD spectra of the SPNEAC/PI nanocomposite showed a sharp and strong diffraction peak at a diffraction angle of 5.6°, which corresponded to a *d*-spacing of 15.78 Å. The *d*-spacing for the clay particles contained in the SPNEAC/PI composites did not change significantly with increasing SPNEAC concentration. An increase of the SPNEAC concentration from 0.5 to 5% (a 900% increase) resulted in a slight decrease in the WAXD diffraction angle from 5.75 to 5.6° (a 2.6% decrease) because of the insertion of PI chains. The intensity of the WAXD diffraction peaks decreased, and the diffraction peak broadened with decreasing SPNEAC loading; this suggested an improved dispersion of SPNEAC in the PI matrix.

SEM

Figure 11(a–d) shows the SEM micrographs of the neat PI and the nanocomposites containing 0.25, 0.5, and 5 wt % SPNEAC at a magnification of 50,000×. At low loadings of SPNEAC (≤0.5 wt %), a dense layered structure was observed. The micrograph of 0.25 wt % SPNEAC–PI [Figure 11(b)] showed a very dense structure. The sample containing about 0.5 wt % SPNEAC, on the other hand, was composed of a dense network of intertwined structures emanating from a second layer. At higher loadings of SPNEAC (≥0.5 wt %), a more open and less compact structure was observed. In Figure 11(d), the emergence of discreet nanoparticles (nodules) throughout the cross-sectional area is shown. These nanoparticles appeared to be loosely arranged inside the PI matrix. On the other hand, the SEM micrograph of neat PI [Figure 11(a)] showed a dense morphology with nanosized cracks.

AFM Analysis

Figure 12 (top and bottom) shows the AFM height profile of the neat PI and the PI containing 5 wt % SPNEAC, respectively. The presence of modified clay and its distribution in the PI matrix was noticeable in the bottom of Figure 12 when compared to the neat PI matrix, shown in the top of Figure 12. On the basis of the AFM micrograph [Figure 11 (bottom)], the microstructure of the SPNEAC–PI nanocomposite showed a homogeneous distribution of filler particles as bright features of about 50 nm to about 220 nm in height and 6.7 μm in length. Also, nanoparticles (nodules) of about 60 nm in height and about 80 nm in length were observed in the nanocomposite containing 5 wt % SPNEAC [Figure 12 (top)]. These nanoparticles (nodules) corresponded to the nodules observed in the SEM micrographs [Figure 12(d)]. The average surface roughnesses of the neat PI and the composite containing 5 wt % SPNEAC were estimated to be about 0.253 nm and about 34.9 nm, respectively. The large difference in surface roughness was attributed to the presence of modified clay particles, which tended to reside on the surface.

CONCLUSIONS

Highly damping PI-based nanocomposite films containing SPNEAC composite were successfully synthesized. Unlike other damping agents, such as elastomeric polymers, which may reduce the strength and thermal stability of the nanocomposite material, the substituted polyaniline-based copolymer improved damping without any significant decrease in the strength or thermal stability of the resulting nanocomposite. The E' values of the samples, which could be correlated with the sample stiffness, was high (~47.8% increase at 0.5 wt %) at low SPNEAC loadings but decreased to a value of 0.93 GPa at 5 wt % at high SPNEAC loadings. The TGA data showed a high char retention of about 60% after 700°C for the nanocomposite; this was comparable to that for neat PI. The area under the α-transition curve, which was correlated with damping and impact energy, increased with SPNEAC loading. This highlighted the significant role played by the SPNEAC copolymer in enhancing the molecular relaxation. The values of impact energy estimated with the α-transition peak, rubbery plateau modulus, and sample volume increased with increasing SPNEAC loading. A 300% improvement in the calculated impact strength for 5 wt % SPNEAC–PI was recorded. T_g of the SPNEAC–PI nanocomposite decreased with SPNEA loading (ca. a 29°C decrease at 5 wt %); this was very significant as far as the processability of the PI-based nanocomposites. AFM studies showed a homogeneous distribution of clay particles and the presence of nodules.

ACKNOWLEDGMENT

This work was supported by National Science Foundation under contract grant number CMMI-0758656.

REFERENCES

1. Lan, T.; Kaviratna, P. D.; Pinnavaia, T. J. *Chem. Mater.* **1994,** *6*, 6573.
2. Huang, J. C.; Zhu, Z. K.; Yin, J.; Qian, X. F.; Sun, Y. Y. *Polymer* **2001,** *42*, 873.
3. Tyan, H. L.; Liu, Y. C.; Wei, K. H. *Chem. Mater.* **1999,** *11*, 1942.

4. Morgam, A. B.; Gilman, J. W.; Jackson, C. L. *Macromolecules* **2001,** *34*, 2735.
5. Agag, T.; Koga, T.; Takeichi, T. *Polymer* **2001,** *42*, 3399.
6. Gu, A.; Kuo, S. W.; Chang, F. C. *J. Appl. Polym. Sci.* **2001,** *79*, 1902.
7. Kim, J. S.; Lee, M. J.; Kang, M. S.; Yoo, K. P.; Kwon, K. H.; Singh, V. R., Min, N. K. *Thin Solid Films* **2009,** *517*, 3879.
8. Giannelis, E. P. *Adv. Mater.* **1996,** *8*, 29.
9. Thomposon, C. M.; Herring, H. M.; Gates, T. S.; Connell, J. W. *Compos. Sci. Technol.* **2003,** *63*, 1591.
10. Tang, Q. Y.; Chan, Y. C.; Wong, N. B. HiTEN **2009**, p 110–115.
11. Li, T. L.; Hsu, S. L. C. *J. Mater. Chem.* **2010,** *20*, 1964.
12. Kong, Y.; Du, H.; Yang, J.; Shi, D.; Wang, Y.; Zang, Y.; Xin, W. *Desalination* **2001,** *146*, 49.
13. Rubal, M.; Wilkins, C. W.; Cassidy, P. E., Jr.; Lansford, C.; Yamada, Y. *Polym. Adv. Technol.* **2008,** *19*, 1033.
14. Tsai, M. H.; Huang, S. L.; Chiang, P. C.; Chen, C. J. *J. Appl. Polym. Sci.* **2007,** *106*, 3185.
15. Yu, Y. H.; Yeh, J. M.; Liou, S. J.; Chen, C. L.; Liaw, D. J.; Lu, H. Y. *Appl. Polym. Sci.* **2004,** *92*, 3573.
16. Yeh, J. M.; Hsieh, C. F.; Jaw, J. H.; Kuo, T. H.; Huang, H. Y.; Lin, C. L.; Hsu, M. Y. *J. Appl. Polym. Sci.* **2005,** *95*, 1082.
17. Seckin, T.; Vural, S.; Koytepe, S. *Polym. Bull.* **2010,** *64*, 115.
18. Zhang, Q.; Naito, K.; Tanaka, Y.; Kagawa, Y. *Macromol. Rapid Commun.* **2007,** *28*, 2069.
19. Liangchai, L.; Ming, W.; Huoming, S.; Haiying, L.; Qingdong, Q.; Yuanlong, D. *Polym. Adv. Technol.* **2001,** *12*, 720.
20. Sua, T. M.; Ballb, I. Conklinc, J.; Huangb, S. C.; Larsonb, R. K.; Nguyenb, S. L.; Lewb, B. M.; Kanerb, R. B. *Synth. Met.* **1997,** *84*, 801.
21. Kuzak, S. G. *J. Appl. Polym. Sci.* **1999,** *73*, 649.
22. Liao, W. H.; Wang, K. W. *J. Sound Vib.* **1997,** *207*, 319.
23. Kishi, H.; Kuwata, M.; Matsuda, S.; Asami, T.; Murakami, A. *Compos. Sci. Technol.* **2004,** *64*, 2517.
24. Pulliam, W.; Lee, D.; Carman, G.; McKnight, G. In Proceedings of SPIE, San Diego; International Society for Optical Engineering: San Diego, CA, **2003;** Vol. 5054, p 360–371.
25. Gou, J.; O'Braint, S.; Gu, H.; Song, G. *J. Nano. Mater.* **2006,** *32803*, 1.
26. Wagner, E. R.; Robeson, L. M. *Rubber Chem. Technol.* **1970,** *43*, 1129.
27. Suhr, J.; Koratkar, N. A.; Keblinski, P.; Ajayan, P. *Nat. Mater.* **2005,** *4*, 134.
28. Liu, A.; Huang, J. H.; Wang, K. W.; Bakis, C. E. J. *Intell. Mater. Syst. Struct.* **2006,** *17*, 217.
29. Woo, L.; Westphal, S.; Ling, M. T. K. *Polym. Eng. Sci.* **1994,** *34*, 420.
30. Wada, Y.; Kasahara, T. *J. Appl. Polym. Sci.* **1967,** *11*, 1661.
31. Gupta, S.; Mantena, P. R.; Al-Ostaz, A. *J. Reinf. Plast. Compos.* **2009,** *29*, 2037.
32. Kuzak, S. G.; Shanmugam, A. *J. Appl. Polym. Sci.* **1999,** *73*, 649.
33. Vincent, P. I. *Polymer* **1974,** *15*, 111.
34. Gupta, A. K.; Purwar, S. N. *J. Appl. Polym. Sci.* **1986,** *31*, 535.